118057 binds to the pore helix and the nearby S6 segment and enhances I_{Kr} currents by attenuating inactivation with little effect on deactivation.

Recently the organic chemical compound ICA-105574 was introduced as a new type of hERG activator (5). Mutagenesis study (6) revealed that the molecular determinant of the binding site was distinct from those of RPR260243 and PD-118057, but had some overlap with them. ICA-105574 shifts the voltage dependence of P-type inactivation to a very positive direction and removes the hERG channel from inactivation at physiological membrane potentials. Although the first report for ICA-105574 (5) showed shortening of action potential duration (APD) in guinea-pig ventricular myocytes, consequences of hERG activation by ICA-105574 in vivo have not been studied. Thus, the goal of the present study was to investigate the effects of ICA-105574 on ECG parameters and monophasic action potentials (MAP) obtained from Langendorff-perfused guinea-pig hearts and anesthetized dogs. In the canine experiments, free drug plasma concentrations were estimated from drug plasma concentrations.

Materials and Methods

Patch-clamp experiments

Patch-clamp experiments were conducted as described previously (7). Briefly, human embryonic kidney (HEK) 293 cells stably expressing the hERG channel (Merck Millipore, Tokyo) were cultured in Minimum Essential Medium supplemented with 10% FBS and 0.5 mg/mL geneticine. hERG channel currents were recorded at room temperature (23°C – 25°C) using the whole-cell patch clamp technique with an Axopatch 200B amplifier (Molecular Devices, Sunnyvale, CA, USA). The control bath solution contained 137 mM NaCl, 4 mM KCl, 1.8 mM $CaCl_2$, 1 mM $MgCl_2$, 10 mM glucose, and 10 mM HEPES, pH 7.4. The drugs were added to the bath solution. Borosilicate glass pipettes (2 – 5 MΩ resistance) were filled with an internal solution containing 130 mM KCl, 1 mM $MgCl_2$, 5 mM EGTA, 5 mM MgATP, and 10 mM HEPES, pH 7.2. Series resistance was 3 – 6 MΩ. Signals were filtered at 5 kHz, sampled at 10 kHz, and compensated for cell capacitance but not series resistance. Unless otherwise noted, hERG currents were elicited at 0.1 Hz with 2-s activating pulses to 10 mV (Vt) followed by 2-s pulses of −50 mV from a holding potential of −80 mV. To obtain concentration–response relationships, the peak current amplitudes at Vt were monitored until current magnitude reached a steady-state level before and after administration of drugs at each concentration. Clampex 9.2 or 10.1 software (Molecular Devices) was used to acquire and analyze data.

Animals

All experiments were performed according to the "Rules for Feeding and Storage of Experimental Animals and Animal Experiments" and approved by the Institutional Animal Care and Use Committee of Mitsubishi Tanabe Pharma Corporation.

ECG and MAP in Langendorff-perfused guinea-pig hearts

ECG and MAP were measured using the previously reported method (8). Hearts were dissected from male Hartley guinea pigs (body weight 380 – 650 g; Japan SLC, Inc., Shizuoka) anesthetized with sodium pentobarbital (50 mg/kg, i.p.; Kyoritsu Seiyaku Co., Tokyo), mounted on a Langendorff apparatus and perfused at approximately 80 mmHg with an aerated Krebs-Henseleit solution. Experiments were carried out with solution temperatures at 37°C ± 0.5°C. Two electrodes were placed, one at the apex of the heart and the other in the aortic cannula, to generate bipolar ECG. MAP was recorded from the epicardium of the left ventricular surface. The right ventricle was paced at approximately 2.5 times the threshold voltage by an electronic stimulator (Fukuda Denshi, Tokyo) via a bipolar electrode attached to its surface. Signals were amplified with differential amplifiers (DAM50 system; World Precision Instruments, Sarasota, FL, USA) and sampled at 1 kHz. Data were acquired and analyzed with WinVAS3 software (Ver. 1.1, Physio-Tech, Tokyo). Corrected QT intervals (QTc) were calculated using three different formulas, Van de Water's [$QTc\ (V) = QT - 0.087\ (RR - 1000)$] (9), Bazett's [$QTc\ (B) = QT/RR^{1/2}$] (10), and Fridericia's formula [$QTc\ (F) = QT/RR^{1/3}$] (11). In MAP recordings, the APD at the 90% repolarization level was defined as MAP_{90}. To stabilize sinus rhythm beating, hearts were perfused for more than 60 min before experimental protocols were started. The evaluation protocol consisted of 20-min perfusion of vehicle [0.1% (v/v) dimethylsulphoxide, DMSO] as the control, followed by cumulative additions of ICA-105574 at final concentrations of 0.3, 1, and 3 μM (20-min perfusion for each). A vehicle only protocol was also run as a time-matched control. Parameters of ECG and MAP were evaluated at the end of each 20-min perfusion. In addition, MAP_{90} was determined under pacing at 300 beats/min (bpm), a rate far above the spontaneous sinus rate. The pacing was also applied at the end of each 20-min perfusion period.

ECG recordings in anesthetized dogs

Surface lead II ECG was measured in four anesthetized male beagles (body weight, 11 – 17 kg) as described previously (12). The dogs were anesthetized initially with 30 mg/kg sodium thiopental, i.v. (Mitsubishi Tanabe

Pharma, Osaka) and maintained in the anesthetized condition with inhalation of 1% halothane (Takeda Chemical Industries, Osaka). The ECG data were acquired with a polygraph system (RM-6000; Nihon Kohden, Tokyo) and recorded on graph paper as well as onto a computer at 1 kHz. Data analysis was performed with software WinVAS3 Ver1.1 (Physio-Tech, Tokyo) or manually using calipers. The ECG parameters studied were spontaneous heart rate, QRS duration, PR, QT, and QTc intervals. ICA was administered at two doses, 1 and 10 mg/kg, as a 10-min intravenous infusion every 30 min and compared with vehicle-only infusion. In two of the four dogs, a 3 mg/kg dose was studied as well. Each ECG parameter was evaluated before the start of infusion and at 5, 10, 15, 20, and 30 min after the start of infusion at each dose. In addition, at the highest dose of 10 mg/kg ICA-105547, ECG parameter evaluation was extended to include the time points 45 and 60 min after the start of the infusion.

Analytic determination of drug exposure

Plasma concentration of the drug was determined in the plasma samples obtained from the same animal in which surface ECG was monitored. Blood was sampled from the femoral vein at 5, 10, 20, and 30 min after the start of drug infusion and additionally at 60 min for the highest dose. The plasma was collected from the supernatant of blood samples except for the vehicle sample after centrifugation at 1500 *g* for 30 min at 4°C and stored at −80°C until the drug concentration was measured. Plasma concentration of ICA-105574 was determined by HPLC (Agilent 1200, Agilent Technologies or CLASS-VP, Shimadzu, Kyoto) and MS/MS (API 3000 or API 5000; AB SCIEX, Foster City, CA, USA). The protein binding ratio of ICA-105574 in canine plasma was determined by a micro-scale ultracentrifugation method (13) using UPLC/MS/MS (Waters, Milford, MA, USA). Estimated free drug plasma concentrations were calculated using the results of the protein binding ratio (98.8%).

Statistics

All values are presented as the mean ± S.E.M. Graphical and statistical analysis were carried out using Origin 8.0J (Microcal, Northampton, MA, USA) or SAS (SAS 9.1.3, SAS Institute, Cary, NC, USA), respectively. Statistical significance was assessed with Student's *t*-test for paired comparisons and adjusted by a Bonferroni method for multiple comparisons, unless otherwise noted. Time-dependent effects of ICA were analyzed in each group using one-way repeated measures ANOVA with the time as the factor of the analysis, followed by a Bonferroni post hoc test. Differences with P value < 0.05 were considered to be significant.

Chemicals

ICA-105574 was synthesized by the Medicinal Chemistry Research Laboratories of Mitsubishi Tanabe Pharma Co. In the in vitro and ex vivo experiments, ICA-105574 was dissolved with DMSO (Sigma-Aldrich, St. Louis, MO, USA) as a stock solution and diluted with bath solution or Krebs-Henseleit solution just before use. The final concentration of DMSO in test solutions was 0.1% (v/v). For the in vivo experiments, ICA-105574 was dissolved with vehicle (10% *N,N*-dimethylacetoamide; Kanto Chemical Co., Inc., Tokyo), 70% polyethylene glycol 400 (Wako Pure Chemical Industries, Ltd., Osaka), and 20% water for injection (Otsuka Pharmaceutical Factory, Inc., Tokushima) up to 10 mg/mL.

Results

ICA-105574 increased hERG currents during the depolarization step

Figure 1 confirms that ICA-105574 synthesized by us activated hERG currents as described previously (5). ICA-105574 enhanced the hERG currents during test pulses to 10 mV in a concentration-dependent manner. The EC_{50} value was estimated as 0.42 ± 0.04 μM with a Hill coefficient (n_H) of 2.5 ± 0.3. The maximal increase in current amplitude (E_{max}) for ICA-105574 was 5.5 ± 0.3–fold greater than the control current. ICA-105574 had little effect on the peak tail currents at −50 mV (Fig. 1A) and at −120 mV (Fig. 1B), and it slowed deactivation as described previously (5).

Analysis of the I-V relationship (Fig. 1B) showed that ICA-105574 enhanced peak hERG currents at test voltages (Vt) more positive than −50 mV (5). Under control conditions, the I-V relationships produced a bell-shape curve (maximal at 0 mV) which reflects the inward rectification of hERG channels resulting from slow activation and fast inactivation (14, 15). ICA-105574 at 2 μM significantly enhanced peak hERG currents at Vt greater than −50 mV and abolished the inward rectification, suggesting that the P-type inactivation was progressively shifted to positive potentials as previously reported (5). As a result, the relative increase in peak currents induced by the activator was more significant at very positive Vt higher than 10 mV. This result implies that ICA-105574 enhances outward cationic currents during the plateau phase of the action potential, resulting in acceleration of ventricular repolarization and shortening of APD.

QT shortening effects of ICA-105574 in guinea pigs

We tested whether ICA-105574 affected ECG and MAP in guinea-pig Langendorff hearts (Fig. 2). ECG or

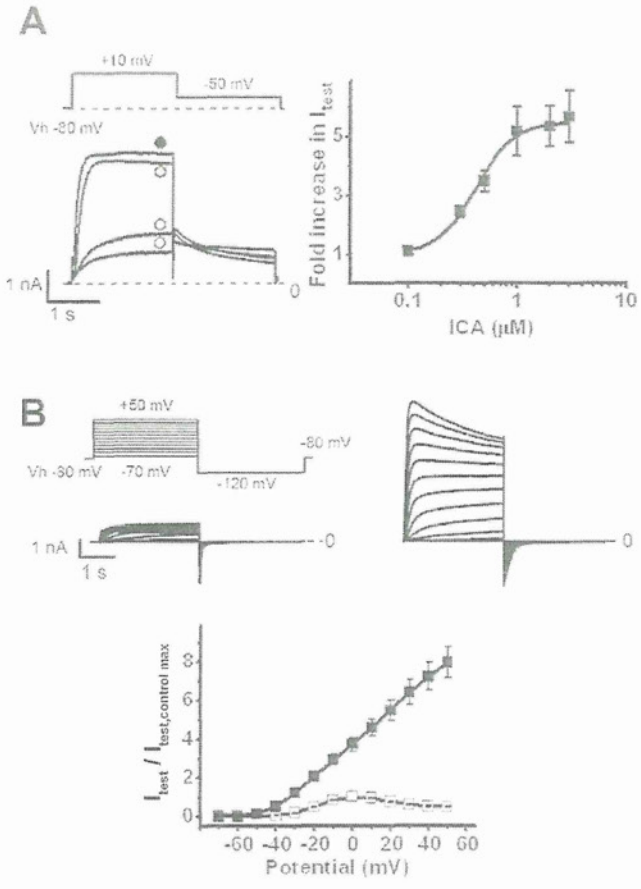

Fig. 1. Effects of ICA-105574 on hERG currents recorded from HEK293 cells stably expressing hERG. A: Concentration-dependent activation of hERG currents by ICA-105574 elicited by 10-mV test pulses (−50 mV return) from a holding potential of −80 mV as indicated above the traces. Shown are representative traces (left) in the absence (control; open circle) and presence of ICA-105574 (0.3 μM: light gray circle, 1 μM: dark gray circle, 3 μM: black circle) and a concentration-dependent curve of hERG activation (right). Plots show the mean ± S.E.M. of peak amplitudes at the test pulses (I_{test}) normalized to control amplitudes before the application of ICA-105574 (n = 5 – 7). Two or three concentrations were tested in a single cell. The curve represents the best fit of data points with a logistic model of nonlinear regression (EC_{50} = 0.42 ± 0.04 μM, n_H = 2.5 ± 0.3). B: Effects of ICA-105574 at 2 μM on the I-V relationship of hERG currents. Membrane currents were elicited by 3-s test pulses to voltages ranging from −70 to +50 mV in 10-mV increments (−120 mV, return) as indicated above the traces. Representative traces in the absence (below voltage protocol) and presence of 2 μM ICA-105574 (upper right) are shown. In the lower panel, the mean ± S.E.M. of normalized amplitude to each maximum amplitude of I_{test} in the absence of the drug are plotted against the test pulse voltages (n = 8).

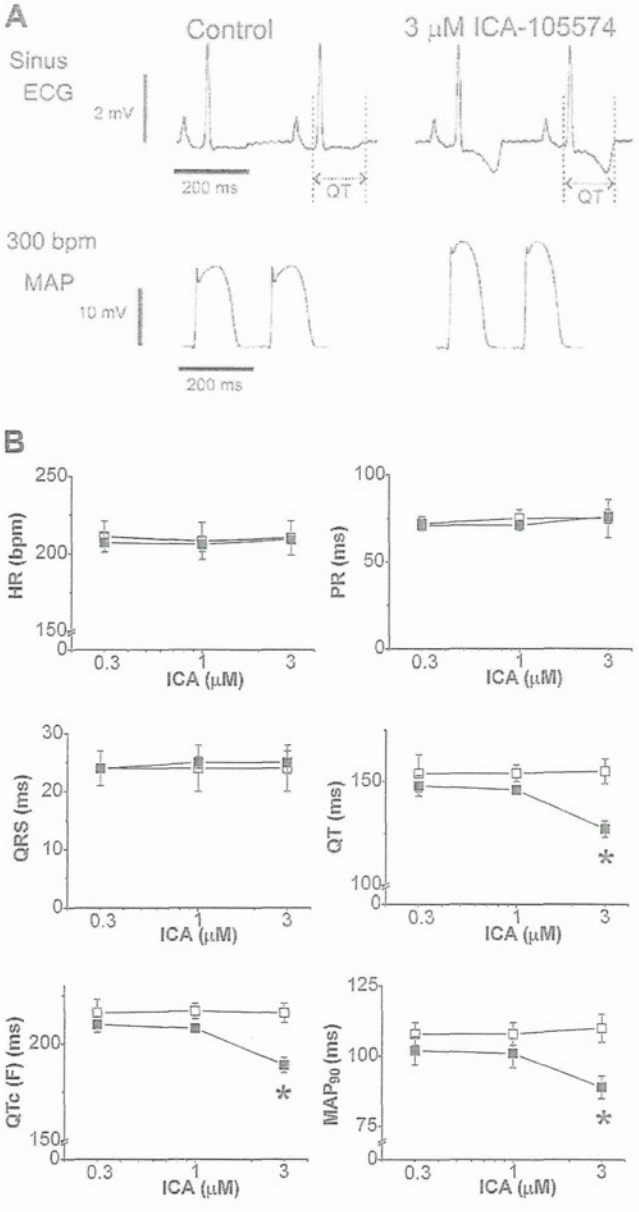

Fig. 2. Effects of ICA-105574 on ECG and MAP recordings from Langendorff perfused guinea-pig hearts. A: Representative ECG and MAP recordings from the same heart pre-treatment (control, left) and after the application of 3 μM ICA-105574 for 20 min (right). Shown are the ECG (upper) during sinus rhythm and MAP_{90} (lower) during ventricular pacing at 300 bpm. B: Effects on ECG parameters and MAP_{90}. ECG parameters after 20-min application of drug (black squares) or vehicle as time-matched control (open squares) were compared to the control value in each heart (n = 5). Error bars represent the S.E.M. PR: PR interval, QRS: QRS width, QT: QT interval, QTc (F): QT interval corrected by the Fridericia formula. *P values < 0.05 according to the unpaired Student's t-test adjusted by Bonferroni's method.

MAP parameters obtained from the Langendorff hearts were stable during vehicle control (0.1% DMSO) perfusion throughout the experiment for more than 80 min. As shown in Fig. 2, at 3 μM, but not at 0.3 or 1 μM, ICA-105574 significantly shortened both QT and QTc (F) intervals and QTc (B) and QTc (V) intervals were as well (data not shown). In addition, MAP_{90} recorded at 300 bpm was also shortened by application of 3 μM ICA-

105574 (P values < 0.05, Student's t-test adjusted by Bonferroni method vs. vehicle control, n = 5). Other ECG parameters such as spontaneous heart rate, PR interval and QRS duration, were not changed. Because the bath solution containing ICA-105574 at concentrations higher than 3 μM produced precipitant in the aerated Krebs-Henseleit solution, we could not increase the concentration to higher than 3 μM.

Effects of ICA-105574 on ECG parameters in anesthetized dogs

To test in vivo effects, we next examined the effects of ICA-105574 on the surface ECG in anesthetized dogs. Typical traces of lead II ECG are shown in Fig. 3A, and the time course of changes in the ECG parameters are plotted in Fig. 3B. Values of ECG parameters are summarized in Table 1. The administration of 1 mg/kg ICA-105574 had no effect on ECG parameters except for an increase in heart rate by 18% of the pre-treatment control (n = 4, $P < 0.05$), similar to that caused by the vehicle (17%, n = 2), probably due to effects of the solvent. Administration of the drug at 3 mg/kg (n = 2) or 1 mg/kg (n = 2) produced no changes. Administration of 10 mg/kg ICA-105574 significantly shortened QT and QTc (V), with a maximal change at 10-min after the start of drug infusion, and significantly increased heart rate by 55% of the pre-treatment control (n = 4, mean from 83 to 121 bpm, $P < 0.01$). The heart rate recorded at 10 mg/kg was higher than that of vehicle (by 17%), indicating that ICA-105574 affected the heart rate at this dose. After infusion of 10 mg/kg ICA-105574 for 5 – 20 min, QTc (V) intervals were maximally shortened by 20% relative to the pre-treatment control, respectively ($P < 0.01$). QTc (B) and QTc (F) intervals were changed as well as QTc (V) (data not shown).

Drug concentration in plasma

The time courses of free plasma concentrations of ICA-105574 are summarized in Fig. 4. The peaks of free drug plasma concentrations were observed at 10-min after the start of infusion (1 mg/kg: 0.16 ± 0.02 μM, n = 4; 3 mg/kg: 0.46 μM, n = 2; and 10 mg/kg: 1.67 ± 0.23 μM, n = 4), corresponding to the time of maximal changes in ECG parameters (Fig. 3).

Discussion

The major finding of this work is that intravenous administration of the novel hERG activator ICA-105574 significantly shortens rate-corrected QT intervals and moderately increases heart rates in anesthetized dogs. This has a major impact on understanding of in vivo effects of hERG activators on cardiac electrophysiology.

A variety of drugs has been reported to cause acquired long QT syndrome through inhibition of the hERG channel. The non-clinical guidance detailed in the International Conference on Harmonization (ICH), S7B suggests that the potential of compounds to interact with I_{Kr} (hERG) and to prolong the QT interval in non-rodent species should be evaluated prior to clinical trials. Compared with the enormous amount of accumulated knowledge on hERG blockers (16), information on the in vivo effects of hERG activators is limited.

At cellular levels, it has been reported that there are at least two types of hERG activators (17). The type 1 activator RPR260243 induces delayed deactivation and a positive shift in the voltage-dependence of inactivation (18, 19). In type 2, PD-118057 (20), its analogue PD-307243 (21), NS1643 (22, 23), and A935142 (24) act primarily to attenuate inactivation. ICA-105574, the drug used in the current study, was initially classified as a type 2 drug because it exhibits a robust depolarizing shift in the voltage dependence of inactivation with modest changes in activation and deactivation (5, 6). Recently, a site-directed mutagenesis study (6) revealed that the binding site on hERG channels for ICA-105574 was distinct from those of RPR260243 (type 1) and PD-118057 (type 2), suggesting that ICA-105574 could be classified as a third type of hERG activator. The binding site for ICA-105574 has overlap with the binding sites of the other two types of activators and with common inhibitors (Y652). Thus, the underlying effects on hERG are expected to vary between classes and between drugs within classes (25).

Selective hERG inhibitors act to delay repolarization and prolong QT intervals on the ECG in vivo at free plasma concentrations comparable to hERG IC_{50}. However, effective potential in vivo is not always comparable to in vitro efficacy for off-target drugs, which have effects on autonomic nervous systems or multiple channels or metabolism, or have indirect effects on the hERG channel such as block of trafficking (16, 26, 27). In the in vivo experiments (Fig. 3), ICA-105574 at a high dose (10 mg/kg) increased heart rates and shortened PR intervals, while ICA-105574 did not affect heart rates and PR intervals in excised Langendorff hearts (Fig. 2). Thus, the autonomic nervous system might be involved in the effects on heart rates and PR intervals possibly by affecting blood pressure (no data). Furthermore, plasma protein binding may affect the effective dose by limiting effective exposure in vivo and should be considered when discussing the correlation between in vitro and in vivo studies. There is little information on this correlation for hERG activators. In the current study, we showed that ICA-105574 shortened QT and QTc intervals in vivo at similar concentrations to which ICA-105574 activates

hERG currents in vitro, suggesting that ICA-105574 is selective for the hERG channel. To our knowledge, this is the first report to show in vivo effects of an hERG-activating compound against validated drug plasma concentrations. The reason that we used anesthetized animals in this study was that stable ECG was obtained continuously under controlled with drug plasma concentrations compared with conscious animals. The halothane probably reduces repolarization reserve through suppression of a slow component of delay rectifiers and the halothane anesthetized dog model has an extent of repolarization thought to be similar to that in healthy human

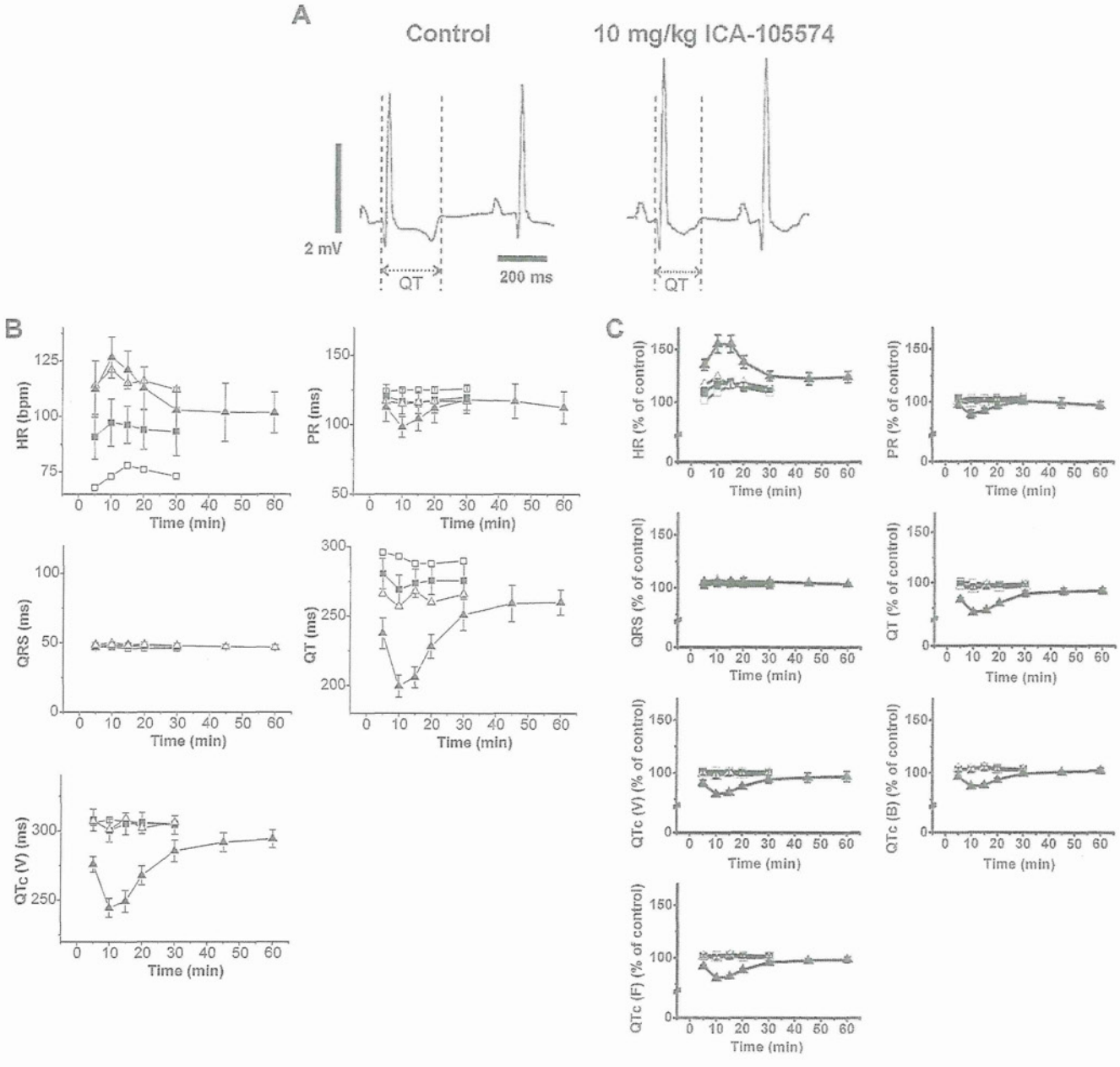

Fig. 3. Effects of ICA-105574 on ECG in anesthetized dogs. A: Shown are representative ECG traces pre-treatment (control) and after 10 mg/kg ICA-105574 intravenous infusion. B: Time-dependent changes in ECG parameters at each time point after vehicle (open squares) or 1 (closed squares), 3 (open triangles), and 10 mg/kg (closed triangles) ICA-105574 administration. Error bars represent the S.E.M. PR: PR interval; QRS: QRS width; QT: QT interval; QTc: corrected QT interval; (V) represent QT interval corrected by Van de Water's formula. The numbers of ECG complexes measured were 4 each for the 1 and 10 mg/kg ICA-105574 administration data and 2 each for the vehicle and 3 mg/kg ICA-105574 administration data. C: Relative changes in ECG parameters in B were calculated by normalizing values of vehicle or ICA-treated to the pre-treatment values in each animal.

Table 1. ECG data of anesthetized dogs

	Control (Pre-treatment)	ICA (1 mg/kg)	ICA (10 mg/kg)	Recovery after ICA (10 mg/kg)
Heart rate (bpm)	83 ± 11	97 ±12*	126 ± 11***	102 ± 11*
PR (ms)	119 ± 8	120 ± 9	105 ± 10*	115 ± 11
QRS (ms)	46 ± 1	47 ± 2	48 ± 2	47 ± 2
QT (ms)	284 ± 12	270 ± 12	200 ± 9***	261 ± 10*
QTc (V) (ms)	305 ± 7	301 ± 10	245 ± 8***	295 ± 8
QTc (B) (ms)	330 ± 15	341 ± 19	288 ± 13***	338 ± 14
QTc (F) (ms)	314 ± 9	315 ± 13	255 ± 10***	310 ± 10

ICA (1 mg/kg), ICA (10 mg/kg): after 10-min infusion of 1 and 10 mg/kg of ICA-105574; Recovery after ICA (10 mg/kg): at 50 min after infusion ended; QTc (V): QT interval corrected for heart rate according to Van de Water formula; QTc (B): QT interval corrected for heart rate according to Bazzett's formula; QTc (F): QT interval corrected for heart rate according to Fridericia formula. Data were expressed as the mean ± S.E.M. *$P < 0.05$, ***$P < 0.001$, one-way ANOVA followed by Bonferroni test vs. control (pre-treatment).

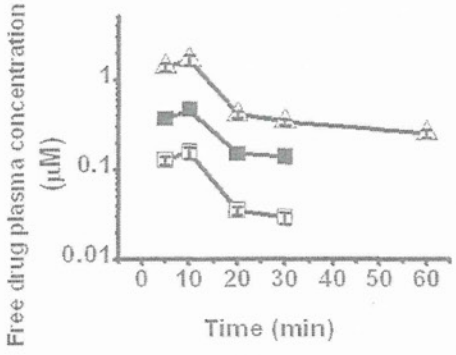

Fig. 4. Estimated free ICA-105574 concentration in canine plasma. The plots show the time course of estimated free ICA-105574 concentration in dog plasma (administration of 1 mg/kg; open squares, 3 mg/kg; closed squares, 10 mg/kg; open triangles). Canine plasma was sampled from the femoral veins of the same dogs in which ECG was measured. Plasma ICA-105574 concentration was determined by the LC/MS/MS method. The protein binding ratio of ICA-105574 in canine plasma was determined by a micro-scale ultracentrifugation method. Estimated free drug plasma concentrations were calculated using the results of this protein binding ratio. All plasma concentrations of ICA-105574 were first obtained as weight concentrations and then converted to molar concentrations (molecular weight, 334.33). The plots were expressed as the mean ± S.E.M. (n = 4) at 1 and 10 mg/kg ICA-105574 and as the mean (n = 2) at 3 mg/kg ICA-105574.

volunteers (28).

As some investigators argued (5), QT shortening by ICA-105574–induced hERG activation might have an impact on the treatment of cardiac arrhythmias associated with long QT intervals, suggesting a potential therapeutic utility of ICA-105574. However, as with the long QT syndromes, the fact that congenital short QT syndromes (29, 30) may lead to susceptibility to arrhythmias raises concerns that QT-shortening drugs could also lead to arrhythmic risk. Although non-clinical data have shown that drug-induced QT and QTc shortening can theoretically lead to ventricular fibrillation and sudden death, the clinical impact of short QT interval is still a matter of debate. The profibrillatory mechanism for short QT is still unclear, although one can speculate that QT shortening causes heterogeneity of repolarization in the heart. Therefore, we have to be careful to use an hERG-channel activator in any patients with electrophysiological disturbances. This study provides an animal model of drug-induced QT shortening caused by hERG activation.

Limitations

Compound solubility issues and the multiple effects of the compound we studied made it more difficult to understand the effects of pure hERG activators in the whole heart.

Therefore, the results were not sufficient to assess our hERG activator's potential for pro-arrhythmia. As a future direction, additional pro-arrhythmic intervention such as extra-pacing or sympathetic nervous stimulations may help to provide evidence for whether hERG activators such as ICA-105574 are pro-arrhythmic or anti-arrhythmic. Because analyzing cardiac dispersion sometimes helps to understand the mechanisms of pro-arrhythmic effects, the data obtained from larger animals, such like dogs in this study, may help provide clues for novel mechanisms.

Acknowledgment

This research was financially supported by the Japan Society for the Promotion of Science (JSPS) through the "Funding Program for World-Leading Innovative R&D on Science and Technology (FIRST Program)" initiated by the Council for Science and Technology Policy (CSTP); Grants from the Ministry of Education, Culture, Sports, Science, and Technology (MEXT) of Japan (23590297 to J.K. and

23390205 to T.F.); and Grants-in-Aid for Scientific Research on Priority Areas (23136503 to J.K.). This work was also supported by a program of support for women researchers from the Tokyo Medical and Dental University. The authors thank Dr. Takekawa and Mrs. Eifuku for measurement of drug plasma concentrations.

References

1 Sanguinetti MC, Jiang C, Curran ME, Keating MT. A mechanistic link between an inherited and an acquired cardiac arrhythmia: HERG encodes the I_{Kr} potassium channel. Cell. 1995;81: 299–307.
2 Clancy CE, Rudy Y. Cellular consequences of HERG mutations in the long QT syndrome: precursors to sudden cardiac death. Cardiovasc Res. 2001;50:301–313.
3 Clancy CE, Kurokawa J, Tateyama M, Wehrens XH, Kass RS. K^+ channel structure-activity relationships and mechanisms of drug-induced QT prolongation. Annu Rev Pharmacol Toxicol. 2003;43:441–461.
4 Brugada R, Hong K, Dumaine R, Cordeiro J, Gaita F, Borggrefe M, et al. Sudden death associated with short-QT syndrome linked to mutations in HERG. Circulation. 2004;109:30–35.
5 Gerlach AC, Stoehr SJ, Castle NA. Pharmacological removal of human ether-a-go-go-related gene potassium channel inactivation by 3-nitro-N-(4-phenoxyphenyl) benzamide (ICA-105574). Mol Pharmacol. 2010;77:58–68.
6 Garg V, Stary-Weinzinger A, Sachse F, Sanguinetti MC. Molecular determinants for activation of human ether-a-go-go-related gene 1 potassium channels by 3-nitro-n-(4-phenoxyphenyl) benzamide. Mol Pharmacol. 2011;80:630–637.
7 Kurokawa J, Tamagawa M, Harada N, Honda S, Bai CX, Nakaya H, et al. Acute effects of oestrogen on the guinea pig and human I_{Kr} channels and drug-induced prolongation of cardiac repolarization. J Physiol. 2008;586:2961–2973.
8 Hamlin RL, Cruze CA, Mittelstadt SW, Kijtawornrat A, Keene BW, Roche BM, et al. Sensitivity and specificity of isolated perfused guinea pig heart to test for drug-induced lengthening of QTc. J Pharmacol Toxicol Methods. 2004;49:15–23.
9 Van de Water A, Verheyen J, Xhonneux R, Reneman RS. An improved method to correct the QT interval of the electrocardiogram for changes in heart rate. J Pharmacol Methods. 1989;22: 207–217.
10 Bazzet H. An analysis of the time relationship of electrocardiograms. Heart. 1920;7:353.
11 Fridericia LS. Die Systolendauer im elektrokardiogramm bei normalen menschen und bei herzkranken. Acta Med Scand. 1920;53:489.
12 Sugiyama A, Hashimoto K. Effects of gastrointestinal prokinetic agents, TKS159 and cisapride, on the in situ canine heart assessed by cardiohemodynamic and electrophysiological monitoring. Toxicol Appl Pharmacol. 1998;152:261–269.
13 Nakai D, Kumamoto K, Sakikawa C, Kosaka T, Tokui T. Evaluation of the protein binding ratio of drugs by a micro-scale ultracentrifugation method. J Pharm Sci. 2004;93:847–854.
14 Schonherr R, Heinemann SH. Molecular determinants for activation and inactivation of HERG, a human inward rectifier potassium channel. J Physiol. 1996;493:635–642.
15 Smith PL, Baukrowitz T, Yellen G. The inward rectification mechanism of the HERG cardiac potassium channel. Nature. 1996;379:833–836.
16 Redfern WS, Carlsson L, Davis AS, Lynch WG, MacKenzie I, Palethorpe S, et al. Relationships between preclinical cardiac electrophysiology, clinical QT interval prolongation and torsade de pointes for a broad range of drugs: evidence for a provisional safety margin in drug development. Cardiovasc Res. 2003; 58:32–45.
17 Perry M, Sanguinetti M, Mitcheson J. Revealing the structural basis of action of hERG potassium channel activators and blockers. J Physiol. 2010;588:3157–3167.
18 Kang J, Chen XL, Wang H, Ji J, Cheng H, Incardona J, et al. Discovery of a small molecule activator of the human *ether-a-go-go-related* gene (HERG) cardiac K^+ channel. Mol Pharmacol. 2005;67:827–836.
19 Perry M, Sachse FB, Sanguinetti MC. Structural basis of action for a human *ether-a-go-go-related* gene 1 potassium channel activator. Proc Natl Acad Sci U S A. 2007;104:13827–13832.
20 Zhou J, Augelli-Szafran CE, Bradley JA, Chen X, Koci BJ, Volberg WA, et al. Novel potent human *ether-a-go-go-related* gene (hERG) potassium channel enhancers and their in vitro antiarrhythmic activity. Mol Pharmacol. 2005;68:876–884.
21 Xu X, Recanatini M, Roberti M, Tseng GN. Probing the binding sites and mechanisms of action of two human *ether-a-go-go-related* gene channel activators, 1,3-bis-(2-hydroxy-5-trifluoromethyl-phenyl)-urea (NS1643) and 2-[2-(3,4-dichloro-phenyl)-2,3-dihydro-1H-isoindol-5-ylamino]-nicotinic acid (PD307243). Mol Pharmacol. 2008;73:1709–1721.
22 Casis O, Olesen SP, Sanguinetti MC. Mechanism of action of a novel human ether-a-go-go-related gene channel activator. Mol Pharmacol. 2006;69:658–665.
23 Hansen RS, Diness TG, Christ T, Demnitz J, Ravens U, Olesen SP, et al. Activation of human ether-a-go-go-related gene potassium channels by the diphenylurea 1,3-bis-(2-hydroxy-5-trifluoromethyl-phenyl)-urea (NS1643). Mol Pharmacol. 2006;69: 266–277.
24 Su Z, Limberis J, Souers A, Kym P, Mikhail A, Houseman K, et al. Electrophysiologic characterization of a novel hERG channel activator. Biochem Pharmacol. 2009;77:1383–1390.
25 Roden DM. Principles in pharmacogenetics. Epilepsia. 2001; 42 Suppl 5:44–48.
26 Shibata S, Okamoto Y, Endo S, Ono K. Direct effects of esmolol and landiolol on cardiac fuction, coronary vasoactivity, and ventricular electrophysiology in guinea-pig hearts. J Pharmacol Sci. 2012;118:255–265.
27 Nishida A, Takizawa T, Matsumoto A, Miki T, Seino S, Nakaya H. Inhibition of ATP-sensitive K^+ channels and L-type Ca^{2+} channels by amiodarone elicits contradictory effect in insulin secretion in MIN6 cells. J Pharmacol Sci. 2011;116:73–80.
28 Takahara A, Sugiyama A, Hashimoto K. Reduction of repolarization reserve by halothane anaesthesia sensitizes the guinea-pig heart for drug-induced QT interval prolongation. Br J Pharmacol. 2005;146:561–567.
29 Bjerregaard P, Nallapaneni H, Gussak I. Short QT interval in clinical practice. J Electrocardiol. 2010;43:390–395.
30 Viskin S, Zeltser D, Ish-Shalom M, Katz A, Glikson M, Justo D, et al. Is idiopathic ventricular fibrillation a short QT syndrome? Comparison of QT intervals of patients with idiopathic ventricular fibrillation and healthy controls. Heart Rhythm. 2004;1: 587–591.

Patient Specific Simulation of Body Surface ECG using the Finite Element Method

JUN-ICHI OKADA, PH.D.,* TERUYOSHI SASAKI, M.SC.,* TAKUMI WASHIO, M.SC.,* HIROSHI YAMASHITA, M.D., PH.D.,† TARO KARIYA, M.D.,† YASUSHI IMAI, M.D., PH.D.,† MACHIKO NAKAGAWA, M.SC.,‡ YOSHIMASA KADOOKA, PH.D.,‡ RYOZO NAGAI, M.D., PH.D.,†,§ TOSHIAKI HISADA, PH.D.,* and SEIRYO SUGIURA, M.D., PH.D.*

From the *Department of Human and Engineered Environmental Studies, Graduate School of Frontier Sciences, The University of Tokyo, Kashiwanoha, Japan; †Department of Cardiovascular Medicine, School of Medicine, The University of Tokyo, Bunkyo-ku, Tokyo, Japan; ‡Fujitsu Ltd., Kawasaki, Kanagawa, Japan; and §Jichi Medical University, Tochigi, Japan

Background: *Recent studies, supported by advances in computer science, have successfully simulated the excitation and repolarization processes of the heart, based on detailed cell models of electrophysiology and implemented with realistic morphology.*

Methods: *In this study, we extend these approaches to simulate the body surface electrocardiogram (ECG) of specific individuals. Patient-specific finite element models of the heart and torso are created for four patients with various heart diseases, based on clinical data including computer tomography, while the parallel multi-grid method is used to solve the dynamic bi-domain problem. Personalization procedures include demarcation of nonexcitable tissue, allocation of the failing myocyte model of electrophysiology, and modification of the excitation sequence. In particular, the adjustment of QRS morphology requires iterative computations, facilitated by the simultaneous visualization of the propagation of excitation in the heart, average QRS vector in the torso, and 12-lead ECG.*

Results: *In all four cases we obtained reasonable agreement between the simulated and actual ECGs. Furthermore, we also simulated the ECGs of three of the patients under bi-ventricular pacing, and once again successfully reproduced the actual ECG morphologies. Since no further adjustments were made to the heart models in the pacing simulations, the good agreement provides strong support for the validity of the models.*

Conclusions: *These results not only help us understand the cellular basis of the body surface ECG, but also open the possibility of heart simulation for clinical applications. (PACE 2013; 36:309–321)*

CRT, computing, electrocardiogram, mapping

Introduction

Recent intense research in cardiac simulation has extended the scope of heart modeling by integrating hierarchical biological components in the heart, ranging from molecules to organs. Development of such a multiscale whole-heart model obviously requires explanation of the different physical principles governing the functional interplay among them.[1,2] With such multiscale, multiphysics features, if successfully implemented, the whole-heart model can be used not only for basic research by extrapolating the knowledge gained at the molecular level and through animal experiments to the behavior of the human heart, but also as a platform for the evaluation of diagnostic tests or the effects of treatment options. However, for the heart models to be truly useful for the latter, that is, for clinical purposes, they must be specific models reproducing the biological characteristics of each patient.

What are the premises for a patient-specific heart model? Although recent diagnostic technologies have provided us with a plethora of data on both morphology and functions to establish and validate the patient-specific heart model, we still consider simulation of the body surface electrocardiogram (ECG) as essential because of its common use in clinical practice as it is less invasive. Furthermore, the important information retrievable from the body surface ECG

This work was supported by the Japan Science and Technology Agency under a grant for Collaborative Development of Innovative Seeds-Practicability Verification Stage, and the Japan Society for the Promotion of Science (JSPS) through its "Funding Program for World-Leading Innovative R&D on Science and Technology (FIRST Program)."

Address for reprints: Jun-ichi Okada, Ph.D., #381 Environmental Building, Kashiwa Campus, The University of Tokyo 5-1-5 Kashiwanoha, Kashiwa, Chiba 277-8563, Japan. Fax: 81-04-7136-4668; e-mail: okada@sml.k.u-tokyo.ac.jp

Received May 17, 2012; revised September 22, 2012; accepted October 23, 2012.

doi: 10.1111/pace.12057

has recently been revisited.[3] In fact, many attempts simulating the ECG based on either a mono- or bi-domain formulation of the cell model for cardiac electrophysiology implemented in image-based models of animal and human hearts have been reported,[4–6] though relatively few studies combine these heart models with an image based torso with various organs segmented to reproduce a realistic ECG.

The major reason for eliminating a realistic torso model from the ECG analysis is the computational cost inherent in such large-scale simulation. Researchers have circumvented this problem by using the boundary element method (BEM) either with the torso (thorax) as the isotropic volume conductor[7,8] or with a realistic torso model using the two step approach. In this approach, *a priori* obtained electrical activity of the heart is mapped onto a coarse torso model and the body surface potential is calculated using either the approximate transfer matrix[5] or a finite element solution.[9] Despite detailed discussion of the convergence and accuracy of these methods,[5,7] we are still unsure whether such approaches ensure clinically approved accuracy for diseased individuals with complex anatomy of both the thorax and heart accompanied by highly variable modes of cardiac excitation and repolarization.

Recently, we developed a method to simulate the human body surface ECG using image-based finite element models of the ventricles and torso, in which various organs are segmented.[10] By applying a multilevel solution technique to a composite mesh consisting of a fine mesh for the heart and a coarse mesh for the torso regions,[11] we solved the large-scale dynamic bi-domain problem in a computationally efficient manner. In the study, we applied this technique to the patient-specific simulation of the body surface ECG. Although the number of subjects studied was small, we were able to successfully reproduce the body surface ECGs for patients under various diseased conditions, thereby showing the potential of this technique for clinical application in the future.

Method

In this study, the clinical data of patients were analyzed retrospectively. The study conformed to the standards set by the latest revision of the *Declaration of Helsinki*, and the protocol was approved by the Ethics Committee of The University of Tokyo. Informed consent was obtained from all patients regarding the use of their clinical data.

Study Subjects

Four patients whose laboratory data, including computer tomography (CT) scans, were available were involved in this study. Profiles of the subjects are given in Table I. Patient #1 had an episode of chest pain, but the clinical investigation revealed no signs of organ abnormalities, and thus he was considered normal. The other three patients suffered from severe congestive heart failure and had undergone implantation of dual chamber pacemakers for cardiac resynchronization therapy (CRT). For these two patients, the data before and after the CRT were analyzed.

Table I.

Patient Characteristics

Patient #	Sex	Age	Diagnosis
1	M	62	chest pain
2	M	73	OMI, p-CABG, CLBBB, CHF, p-CRT
3	M	65	HCM (dilated phase), CHF, p-CRT
4	M	26	AR (p-AVR), CHF, Marfan syndrome susp

OMI = old myocardial infarction; p-CABG = status after cardiac artery bypass graft; CLBBB = complete left bundle branch block; CHF = congestive heart failure; p-CRT = status after the implantation of cardiac resynchronization therapy device; HCM = hypertrophic cardiomyopathy; AR = aortic regurgitation; p-AVR = status after aortic valve replacement; susp: suspect of.

Finite Element Model

Details of finite element models of the human heart and torso have previously been reported.[10,11] As in these previous studies, only the ventricles were modeled and the human ventricular myocyte model of electrophysiology by Ten Tusscher et al. was adopted.[12,13] In addition to the three cell types, that is, endocardial, M-, and epicardial cells, a Purkinje network with high conduction velocity was modeled on the endocardial surface. The average size of each element of the heart model was 0.4 mm but, due to the dilatation of the diseased hearts, the number of elements ranged from 25,067,520 to 64,000,000. We mapped the fiber orientation to each model. However, because there is no available technique for measuring the fiber orientation of beating hearts, we applied the same orientation obtained from the literature (http://gforge.icm.jhu.edu/gf/project/dtmri_data_sets/). For patient #3, a CT scan was performed only for the heart region, and thus a part of the thorax on the right hand side was excluded. Because no deformity was found on the chest X-ray, we constructed the torso model by substituting the missing part with a mirror image of the left hand side of the chest.

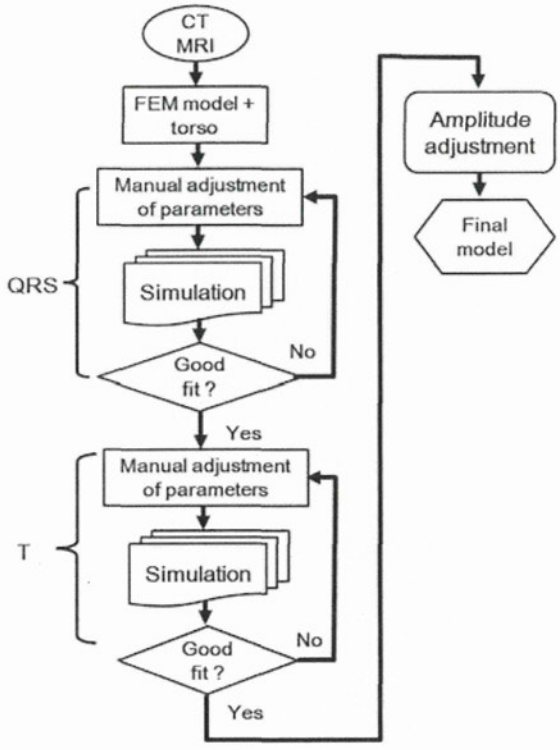

Figure 1. *Workflow showing the simulated ECG fitted to the actual ECG. We adopted a stepwise strategy to sequentially adjust QRS complexes, T waves, and their amplitudes.*

Patient Specific Adjustments to the Model

Patient specific adjustments were made to these models in three steps (Fig. 1). First, we mapped the infarcted region identified by the Tl scintigram where applicable. The region of the permanent defect in perfusion was demarcated and projected onto the heart model as an area of transmural infarction, lacking electrical activity (nonexcitable tissue). However, because Tl scintigram (SPECT) data only provide a coarse map of the infarcted region, we made minor changes to the initially mapped region during ECG matching. In this study, the gray zone between the nonischemic and infarcted region was not considered, owing to the low spatial resolution of the scintigram.

In a previous study, we found that variations in the distribution of cell types with different action potential duration (APD) either in the transmural or apico-basal direction do not change the QRS morphology appreciably (see Fig. 4 in Okada et al.[10]). Accordingly, in the next step, we adjusted the QRS morphology prior to adjusting the distribution of these cell types. Starting from the baseline morphology of the conduction system, which realizes a normal sequence of excitation,[10,14] we shifted the earliest sites of excitation on the endocardium by modifying the distribution of the free-running part of the conduction system to find optimal sites for each patient. To facilitate this procedure, we calculated the instantaneous depolarization (QRS) vector (depicted by arrows in the time-lapse images of the torso in Fig. 3) as the sum of the local excitation vectors in the heart (depicted by small arrows in the time lapse images of the heart in Fig. 2) and simultaneously visualized these in the torso and heart models, respectively (see also the supplementary movie S1). By interactively considering the relationship between the excitation propagation in the heart and the accompanying changes in magnitude and direction of the depolarization vector at any desired moment via the guidance of simultaneously visualized ECGs, the optimal sequence of excitation could be estimated in an efficient manner. Third, the distribution of different cell types was adjusted to reproduce the patient specific T-wave morphologies. Again, for a normal heart, the cell distribution identified in our previous study[10] was applied. The adjustment strategy for a failing heart was based on the two studies. Recently, Glukhov et al. reported that while myocytes with a long APD, presumably M cells, are clustered on the endocardial side in normal human ventricles, such heterogeneity in the APD disappeared in a failing myocardium.[15] Accordingly, for a diseased myocardium, we allocated a single type of failing myocyte model proposed by Winslow et al.,[16] in which the reduction of IK1 and Ito currents, down regulation of the SR Ca^{2+}-ATPase, and up regulation of the Na^{+}-Ca^{2+} exchanger were introduced. The region of the failing myocardium was adjusted according to the patient ECG.

Finally, the thickness of the subcutaneous fat tissue was adjusted to optimize the amplitudes of the ECG waves if necessary.

To facilitate the evaluation of agreement, we also calculated the cross-correlation ($-1 \leq R_{NCC} \leq 1$) between the simulated and actual ECG using the following equation

$$R_{NCC} = \frac{\sum_{j=1}^{12}\sum_{i=1}^{N} A(i,\ j) \times B(i,\ j)}{\sqrt{\sum_{j=1}^{12}\sum_{i=1}^{N} A(i,\ j)^2 \times \sum_{l=1}^{12}\sum_{k=1}^{N} B(k,\ l)^2}},$$

where $A(i,j)$ and $B(i,j)$ are the voltages at time i for the simulated and real ECGs with summation over 12 leads ($j = 1$ to 12). Evaluations were carried out for QRS complexes and entire waves.

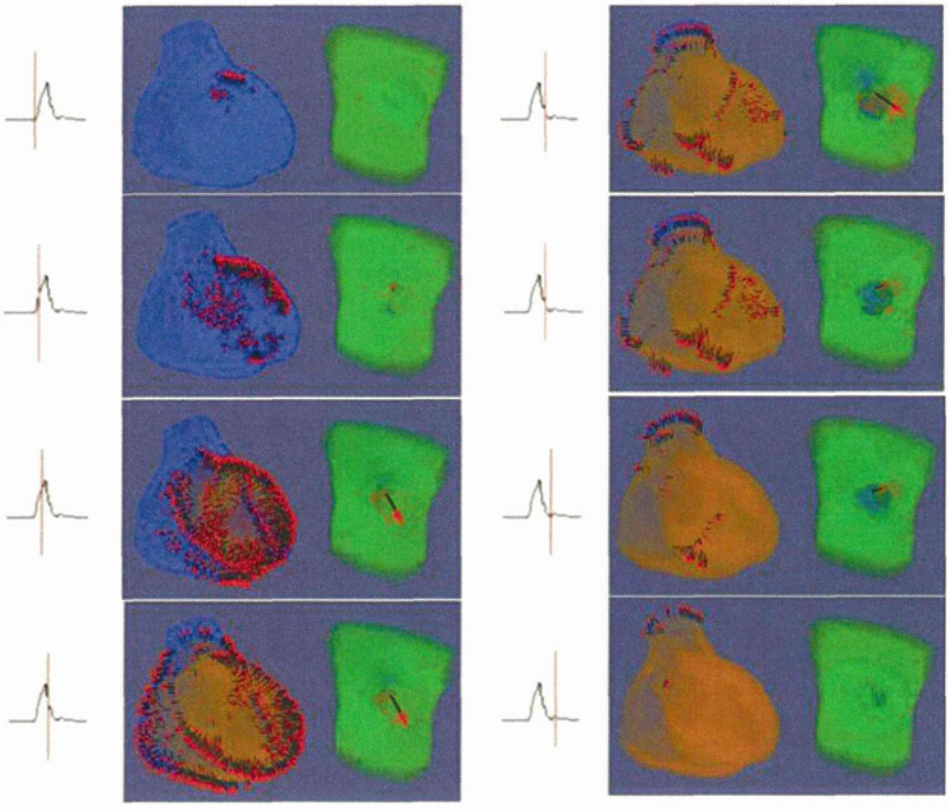

Figure 2. *Visualization of the instantaneous local excitation vectors (small arrows on the heart models), depolarization vector (large arrows on the torso models), and the corresponding ECG (left) for the estimation of excitation sequence. Data for patient #1 at different times from the onset of the QRS complex are shown as time-lapse images. For clarity, only a single lead of the ECG (II lead) is shown and the arrangement of each panel differs from the original computer display.*

Computation

All the program code was written in FORTRAN in our laboratory. Simulations were performed using an SGI Rackable C2108-TY10 server (Intel Xeon X5690 [3.46 GHz], Intel, Santa Clara, CA, USA). With the total number of degrees of freedom set to three hundred million, it took 6 hours to compute a single cardiac cycle. The numerical data was visualized using commercial software (MicroAVS: Advanced Visual Systems, Waltham, MA, USA, and Avizo: VSG, Burlington, MA, USA).

Results

Heart models with and without non-excitable regions for all the patients are shown together with the corresponding torso models in Figure 3. In the hearts of patients #2 and #3, the regions of nonexcitable tissue are indicated below. The size and shape of the heart and torso varied considerably among the patients. The results of the simulations are described separately for each patient.

Patient #1

Since no organ abnormalities were reported for this patient, only the sequence of excitation propagation was adjusted. As for the optimization of the distribution of cell types, no adjustment was made in this case. With these settings, the activation and repolarization sequences of the heart (Fig. 4A) and the resulting changes in the body surface potential (Fig. 4B) were computed fairly rapidly (see also the supplementary movie S2). The simulated ECG with narrow QRS complexes and positive T waves in most of the leads corresponds well with the actual one (Fig. 4C).

Patient #2

According to the information from the scintigram, infarcted regions were set (Fig. 3 center

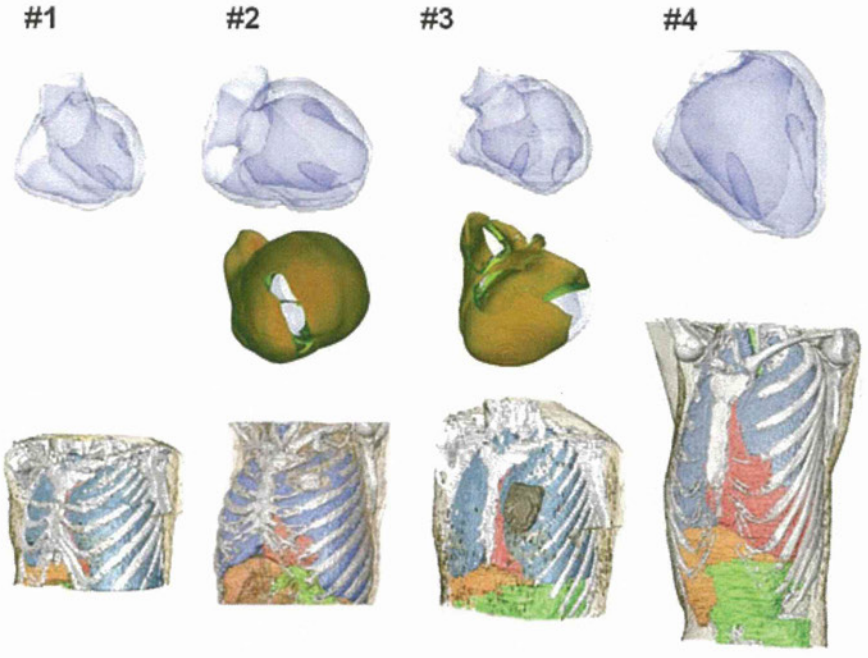

Figure 3. *Finite element models of the heart and torso for the patients studied. For patients #2 and #3, non-excitable regions are shown under the heart models. Scales are different for the heart and torso models, but the same for all patients for ease of comparison.*

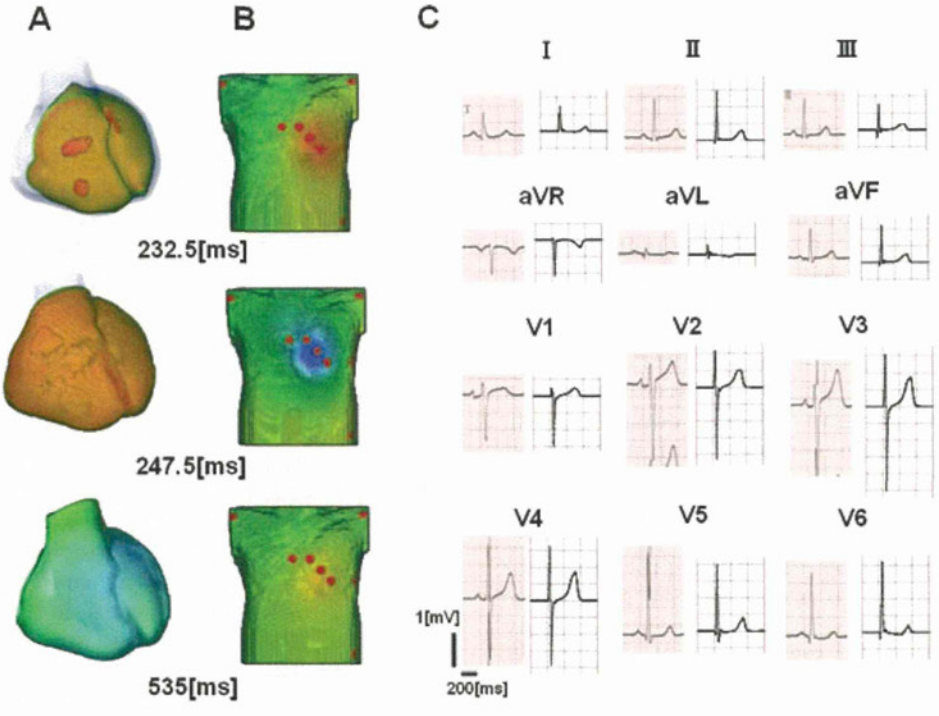

Figure 4. *Propagation of excitation and repolarization (A), body surface potential map (B) as time lapse images, and ECG for patient #1 under control conditions. In (C), the simulated ECG is shown on the right and the actual ECG on the left for each lead. The red dots on the torso (B) represent the ECG leads.*

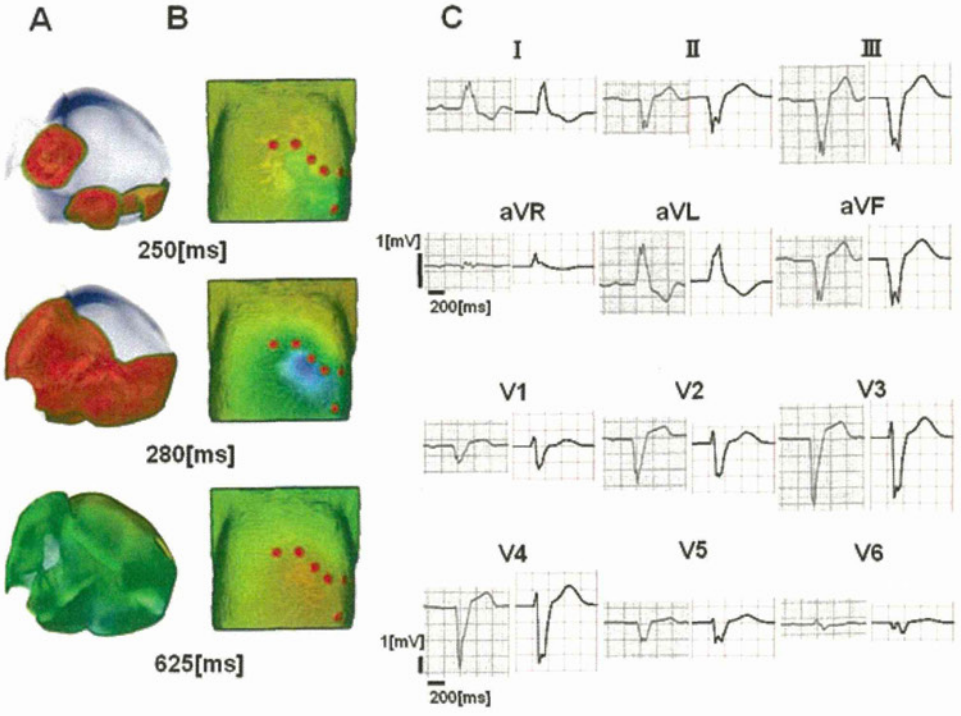

Figure 5. *Propagation of excitation and repolarization (A), body surface potential map (B) as time lapse images, and ECG for patient #2 under control conditions. In (C), the simulated ECG is shown on the right and the actual ECG on the left for each lead. The red dots on the torso (B) represent the ECG leads.*

panel). Based on the clinical diagnosis of a complete left bundle branch block (CLBBB), the earliest excitation sites were eliminated from the left ventricular endocardium and the failing myocyte model was applied to the entire ventricle. Time-lapse images of the membrane potential and body surface potential are shown in Figure 5A and B (see also the supplementary movie S3), while a comparison of the ECGs is presented in Figure 5C. Again, reasonable agreement is observed. Based on the history of the patient's current illness, a CRT device was implanted. We placed the pacing leads at the site of actual implantation determined from the CT images to simulate the CRT. Although a simultaneous bi-ventricular pacing protocol (no inter-ventricular delay) was programmed for this patient, we needed to advance the right ventricular (RV) stimulation by 70 ms to achieve reasonable agreement in the ECGs. In our opinion, this delay can be accounted for by the electrical latency during left ventricular (LV) stimulation from the coronary veins[17] and in fact, a comparison of the ECGs for RV and LV pacing alone supports this idea (Fig. 6C inset). The mode of excitation under CRT is shown in Figure 6A and B (see also the supplementary movie S4), with a comparison of ECGs presented in Figure 6C. Because we did not modify the morphology of the heart and its tissue characteristics determined for the baseline ECG, that is, as shown in Figure 5, the good correspondence after the CRT serves as an independent test for the validity of the model.

Patient #3

In this patient with a dilated phase of hypertrophic cardiomyopathy, an extended and irregular area of perfusion defect is observed in the scintigram. The ECG shows an extremely complex pattern of excitation that differs from the typical CLBBB pattern (Fig. 7C), and this led to a long series of iterative adjustments of both the defect region and earliest excitation sites. In the beginning, the failing myocyte model was allocated to the entire ventricle but, to reproduce the upright T waves in the right precordial leads (V1-V3), we introduced the endocardial, M-, and epicardial cell models transmurally. Final results of the activation sequences and a comparison of the ECGs are shown in Figure 7 (and also in the supplementary movie S5). Although disagreements are seen in some segments, the overall pattern of the complex ECG is well

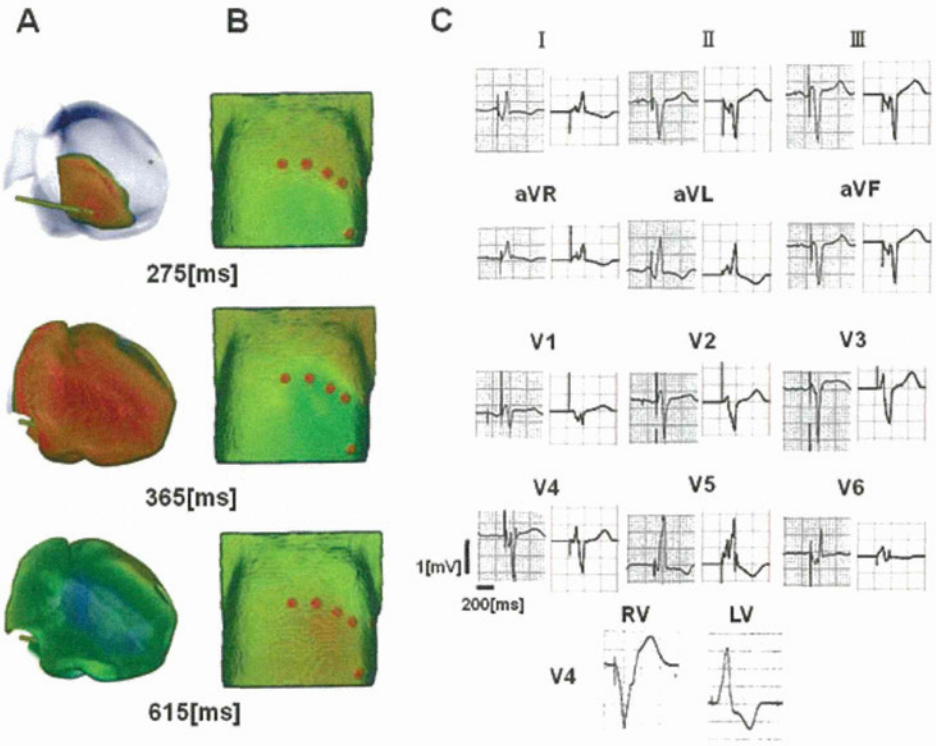

Figure 6. *Propagation of excitation and repolarization (A), body surface potential map (B) as time lapse images, and ECG for patient #2 under bi-ventricular pacing. In (C), the simulated ECG is shown on the right and the actual ECG on the left for each lead. The red dots on the torso (B) represent the ECG leads, and the stick in the heart chamber (A) represents the right ventricular pacing lead. Inset: V4 leads for this patient under RV and LV pacing. A significant delay between the stimulus spike and QRS wave is observed for LV pacing.*

reproduced. The ECG after the CRT was also simulated for this patient according to clinical records, and, as illustrated in Figure 8 (and also in the supplementary movie S6), it shows reasonable agreement with the actual one. Because no further adjustment was made to the baseline model in this case either, the good agreement can be taken to indicate that the modeling may not be unique, but is at least a close solution to this inverse problem.

Patient #4

The heart of this patient was severely dilated because of aortic regurgitation. Duration of the QRS complex was elongated (>140 ms), but the presence of a Q wave in the V6 lead excluded the diagnosis of CLBBB (Fig. 9C). Accordingly, we considered that the widening of the QRS was caused simply by the enlargement of the heart and we started making adjustments from the normal activation sequence, similar to the procedure for patient #1. However, because the duration of the QRS complex was not comparable with the actual data, we reduced the conduction velocity by 68% in the fiber direction and 25% in the cross fiber direction. The final data for excitation propagation, body surface potential, and the ECG are shown in Figure 9, together with the actual ECG for comparison. Once again a reasonable match was achieved (see also the supplementary movie S7). However, under pacing conditions, there is a slight disagreement in the QRS morphology in leads I and VL (Fig. 10) (see also the supplementary movie S8). Such disagreements could be corrected by adjusting the property of the heart model determined under control conditions. Nevertheless, this was not done, owing to a lack of clinical data to rationalize it.

Cross-Correlation

Figure 11 shows an example of the relation between the cross-correlation and the matching of ECG wave form with the corresponding excitation propagation sequence. Each vector in each panel corresponds to the ECG amplitude in the specific lead with the same angle as that in the inset

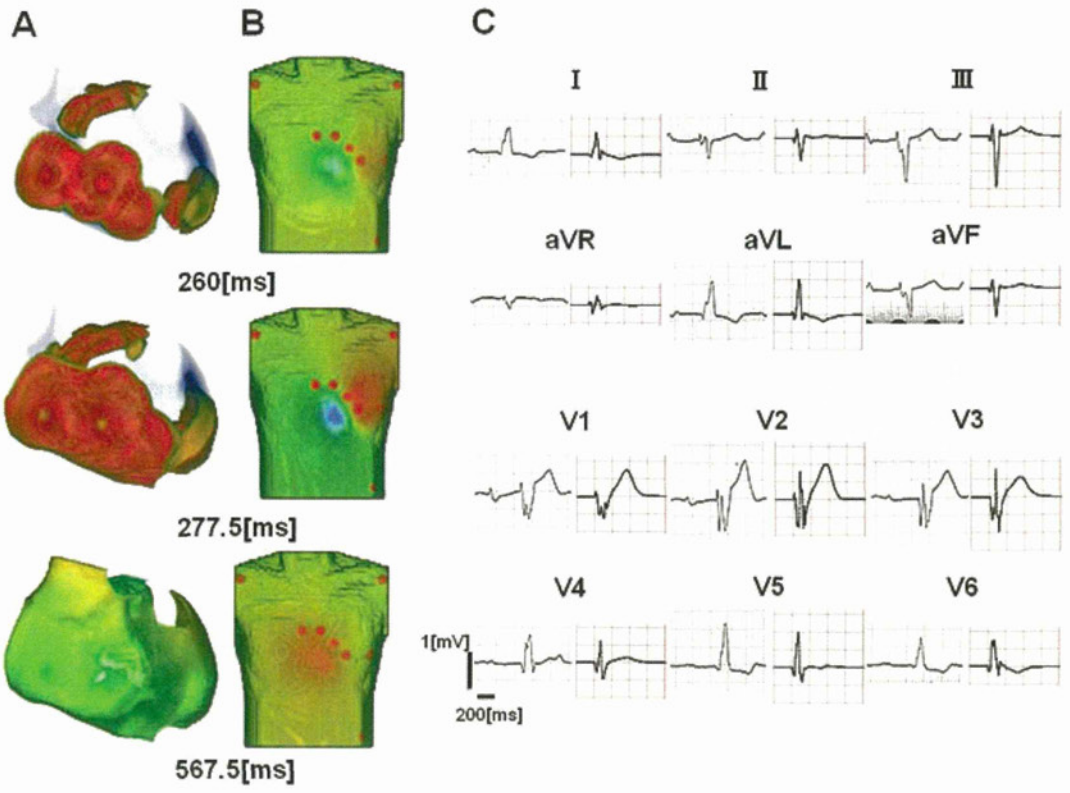

Figure 7. *Propagation of excitation and repolarization (A), body surface potential map (B) as time-lapse images, and ECG for patient #3 under control conditions. In (C), the simulated ECG is shown on the right and the actual ECG on the left for each lead. The red dots on the torso (B) represent the ECG leads.*

at a certain time. Therefore, the similarity of the vector clusters indicates a correct fit of the ECG waveform. Compared with the actual ECG data (top row), the vector cluster in simulation A (middle row) differs significantly at all time points, yielding a cross-correlation value of 0.615. A shift in the earliest excitation sites in simulation B (bottom row) reproduced large upward vectors observed in the actual ECG and increased the cross-correlation to 0.896. For visibility only the precordial vectors are shown; however, limb lead vectors were also taken into consideration. Table II summarizes the cross-correlation of the simulated ECGs for all cases studied (Figs. 4 to 10). Fairly good correlations (>0.65) were obtained for both the baseline and pacing conditions, except for that under pacing in case 2.

Discussion

With the advent of high performance computers, realistic simulation of cardiac electrophysiology, in which cell models of electrophysiology are implemented in the image based finite element models of the heart, is now possible. However, a limited number of attempts have been made with respect to patient-specific ECG simulations coupled with image-based torso models. In this study, although our preliminary approach yielded promising results, we also identified problems to be overcome in future studies.

Patient-Specific ECG Simulation

An alternative approach to the realization of patient specific ECG simulation is, of course, solving the inverse problem, which researchers have pursued for several years.[3,5,18–20] Hitherto, attempts have been successful only in the estimation of epicardial maps,[3] owing to the well-known ill-posed nature of the problem. However, the forward problem approach adopted in this study can provide information on the activation and repolarization sequences within the wall, but this requires iterative simulations with manual adjustment of the parameters. To reduce the computation time required for such repeated ECG simulations, various solution techniques have been proposed, including the BEM[7] and finite element method based on the two step approach.[9] In this study, we used our previously proposed parallel multi-grid method[11] to solve the dynamic

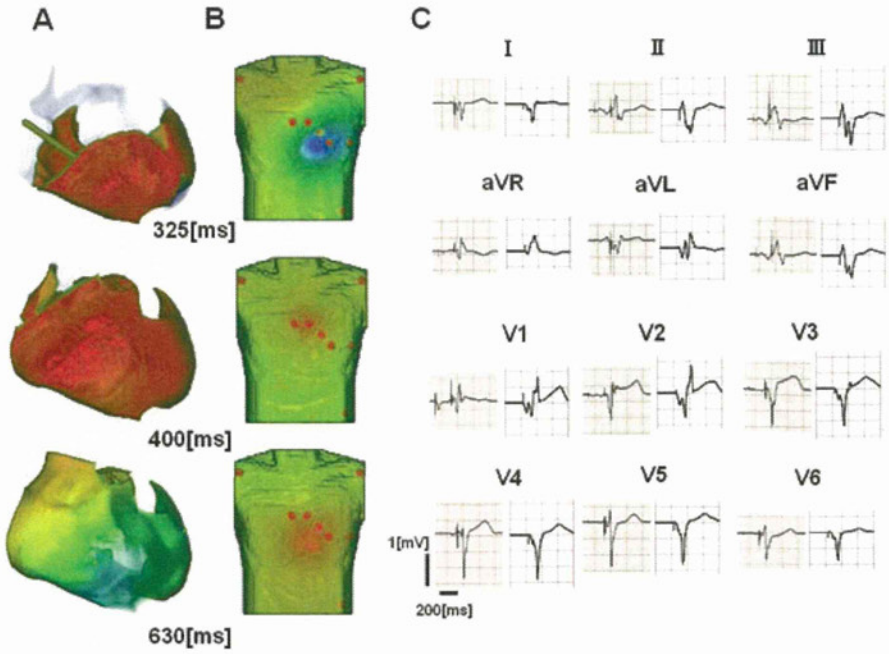

Figure 8. *Propagation of excitation and repolarization (A), body surface potential map (B) as time lapse images, and ECG for patient #3 under bi-ventricular pacing. In (C), the simulated ECG is shown on the right and the actual ECG on the left for each lead. The red dots on the torso (B) represent the ECG leads, while the stick in the heart chamber (A) represents the right ventricular pacing lead.*

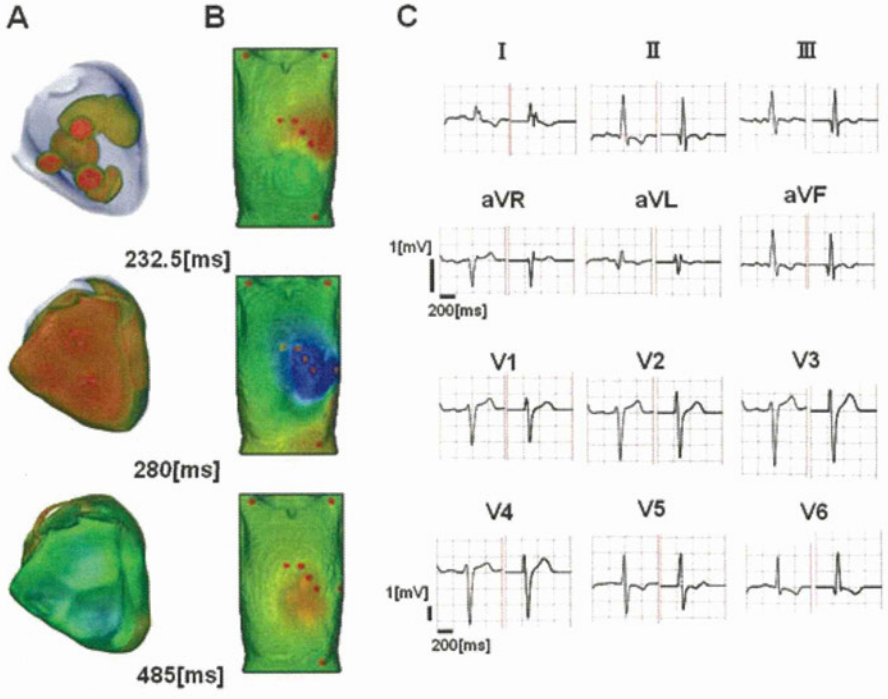

Figure 9. *Propagation of excitation and repolarization (A), body surface potential map (B) as time lapse images, and ECG for patient #4 under control conditions. In (C), the simulated ECG is shown on the right and the actual ECG on the left for each lead. The red dots on the torso (B) represent the ECG leads.*

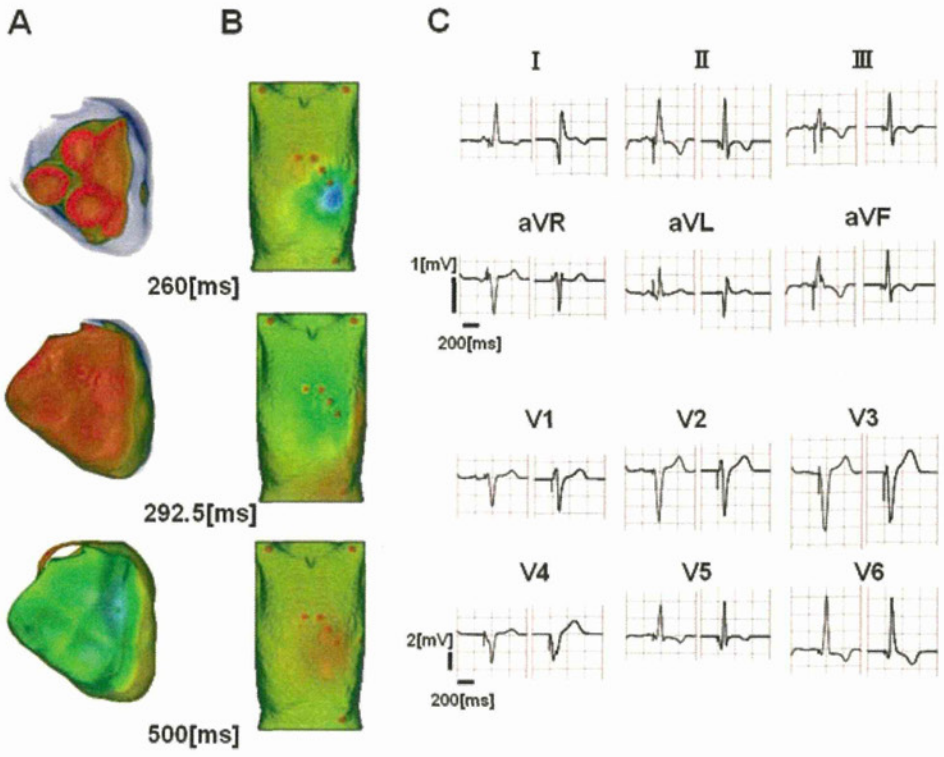

Figure 10. *Propagation of excitation and repolarization (A), body surface potential map (B) in time lapse images, and ECG for patient #4 under bi-ventricular pacing. In (C), the simulated ECG is shown on the right and the actual ECG on the left for each lead. The red dots on the torso (B) represent the ECG leads while the stick in the heart chamber (A) represents the right ventricular pacing lead.*

bi-domain problem within a practical time interval (~80 min). One of the advantages of this approach is its ability to evaluate the influence of surrounding tissue on the electrical activity of the heart, although this influence was not evaluated in this study. We also developed an interactive system for the simultaneous visualization of 3D wave fronts and the vector ECG to accelerate the adjustment of the excitation sequences to reproduce the QRS wave morphology. Even with such developments, however, the total time required to model the complex ECG for patient #2 was quite long. A hybrid approach using both the inverse and forward problems may help in providing a more efficient solution.

Goodness of Fit

To quantify the goodness of fit, we calculated the cross-correlation between the simulated and actual ECGs to obtain reasonable values. However, such neutral numerical indices may not correlate with the visual impression and in fact, clinical diagnosis relies on the characteristic morphology of each segment of the ECG. Furthermore, we cannot be sure whether the morphological fit ensures validity of the parameters set in the model in the absence of clinical measures for direct comparison. However, reproducibility of the model can be evaluated by referring to other clinical data. In this sense, our simulation of the ECG after the CRT implantation (Figs. 6, 8, and 10, and Table II) provides strong support for the validity of our modeling.

Limitations

Although the number of cases in this study was small, the diversity in pathology could suggest potential applicability of this technique to a wide range of diseased hearts. However, cases in which mutant ion channels are expected to have a complex effect on the electrophysiology were not included, and this is left for future study.

The current simulation based on the available clinical data includes many uncertainties in the modeling of both the heart and the torso. Fiber orientation is known to have a significant

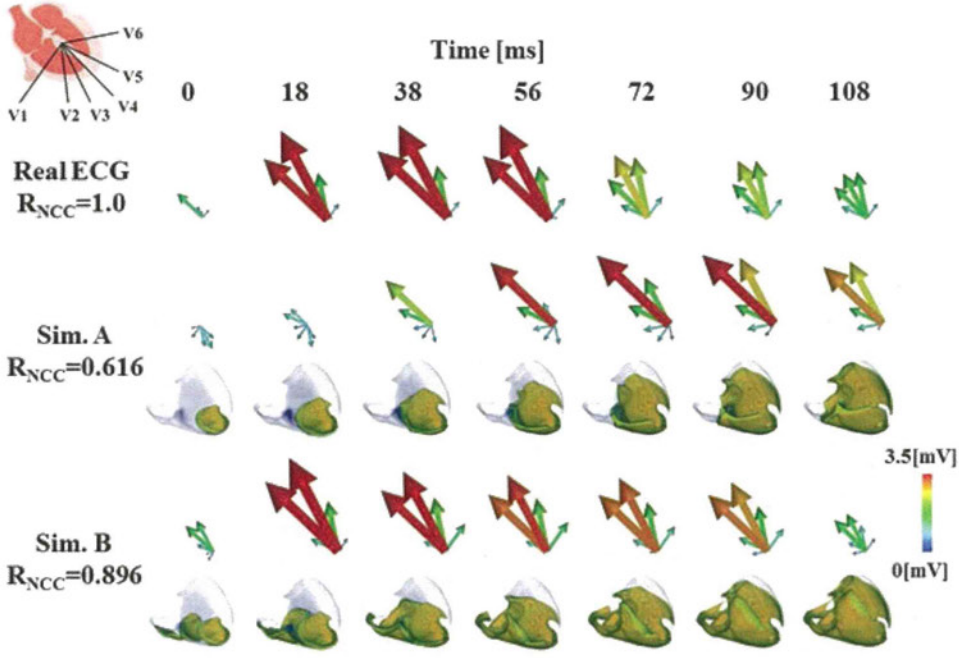

Figure 11. *Sequential changes in ECG vector and ventricular excitation. In each panel, each vector represents the amplitude of the specific precordial lead as indicated in the inset. Top row: actual ECG, and middle and bottom rows: simulation results with poor (Sim. A R_{NCC} = 0.615) and good (Sim. B R_{NCC} = 0.896) cross-correlations, respectively, for case #2. For the simulation results, the accompanying ventricular excitation of the models is shown. The numbers at the top indicate the time since the onset of the QRS complex.*

influence on the conductivity and mechanics of the myocardial tissue.[21–23] Since there is no measure for recording the fiber orientation in a beating heart, we had to adopt the only published data for both normal and diseased hearts. The use of the scintigram absolutely limited the segmentation of myocardial tissue in terms of space and character. We intend to use magnetic resonance imaging (MRI) data with enhancements for the modeling, but even with this information, fine-tuning of the cell model to reproduce reality will be difficult. As an approximation, we used a single parameter set for both the normal and failing myocyte models.[12,16,24]

Uncertainties were also identified in the torso. Dössel's group reported that fat is important in the morphology of the ECG, yet its conductivity varies considerably in the literature.[9,25] However, we also noted that such variation in conductivity scales the waveform, while retaining the overall characteristics. Accordingly, we adjusted the conductivity of the subcutaneous fat tissue to adjust the amplitudes of the ECG; however, further refinement of the model for each patient based on conductivity metric is needed. The influences of variation in myocardial conduction velocity and slowing or blockage in the His-Purkinje system are also important issues that need to be addressed in future studies incorporating cutting edge experimental results.

Furthermore, in this study, we simulated only the electrical activity with a static heart model; however, the feedback influence of mechanical activity on the electrical activity of the heart is well established and simulations taking into account such effects have been reported.[26–29]

Finally, although the calculation of the cross-correlation coefficient shows that the presented results are the best from the models tested, they do not ensure optimality of the model. This is because of the inclusion of the manual iteration part in the

Table II.

Cross-correlation

Case	1	2	3	4
Baseline	0.748	0.896	0.645	0.795
Pacing		0.653	0.579	0.842

procedure, which should be automated in future studies.

Future Directions

To extend the applicability of ECG simulation to a wider range of diseases at various stages, modeling of the atria, coronary circulation, and other anatomical structures coupled with the integration of multiphysics phenomena is necessary. However, such detailed modeling necessitates the development of diagnostic techniques enabling in vivo recording of the micro-anatomical structure, tissue properties, and metabolism. Detailed simulations also require acceleration of the modeling process at each stage. Parametric modeling is a powerful approach,[30] but the final fine-tuning still remains for personalized models. Further studies and developments are clearly needed.

Despite its long history, the inverse problem approach still cannot provide a unique solution for the determination of multiple activation sites or the sequence of transmural activation even when utilizing the body surface mapping data. Alternatively, we adopted the forward problem approach in this study to obtain 3D pattern excitation and repolarization sequences, which reproduces an ECG with reasonable agreement. The number of trials may not be large enough to ensure convergence, but, acceleration of the simulation using a high performance computer will allow us to perform a true exhaustive search to determine the best-fit result in the near future.

Conclusions

We have created patient specific models of the heart and torso for patient-specific simulation of the body surface ECG based on clinical data to successfully reproduce the patient's characteristics. The good agreement obtained for the ECGs under bi-ventricular pacing provides strong support for the validity of the models. The current simulation results not only help us to understand the cellular basis of the ECG, but also open the possibility of an integrative heart simulator for clinical applications.

References

1. Lee J, Niederer S, Nordsletten D, Le Grice I, Smaill B, Kay D, Smith N. Coupling contraction, excitation, ventricular and coronary blood flow across scale and physics in the heart. Phil Trans R Soc A 2009; 367:2311–2331.
2. Trayanova NA. Whole-heart modeling applications to cardiac electrophysiology and electromechanics. Circ Res 2011; 108:113–128.
3. Ramanathan C, Ghanem RN, Jia P, Ryu K, Rudy Y. Noninvasive electrocardiographic imaging for cardiac electrophysiology and arrhythmia. Nature Medicine 2004; 10:422–428.
4. Potse M, Dubé B, Richer J, Vinet A, Gulrajani RM. IEEE Trans Biomed Eng 2006; 53:2425–2435.
5. Farina D, Jiang Y, Dössel O. Acceleration of FEM-based transfer matrix computation for forward and inverse problems of electrocardiography. Med Biol Eng Comput 2009; 47:1229–1236.
6. Vigmond E, Vadakkumpadan F, Gurev V, Arevalo H, Deo M, Plank G, Trayanova N. Towards predictive modelling of the electrophysiology of the heart. Exp Physiol 2009; 94:563–577.
7. Fischer G, Tilg B, Modre R, Huiskamp GJM, Fetzer J, Rucker W, Wach P. A bidomain model based BEM-FEM coupling formulation for anisotropic cardiac tissue. Ann Biomed Eng 2000; 28:1229–1243.
8. Xue J, Gao W, Chen Y, Han X. Study of repolarization heterogeneity and electrocardiographic morphology with a modeling approach. J Electrocardiol 2008; 41:581–587.
9. Keller DUJ, Weber FM, Seemann G, Dossel O. Ranking the influence of Tissut conductivities on forward-calculated ECGs. IEEE Trans Biomed Eng 2010; 57:1568–1576.
10. Okada J, Washio T, Maehara A, Momomura S, Sugiura S, Hisada T. Transmural and apicobasal gradients in repolarization contribute to T-wave genesis in human surface ECG. Am J Physiol 2011; 301:H200–H208.
11. Washio T, Okada J, Hisada T. A parallel multilevel technique for solving the bidomain equation on a human heart with Purkinje fibers and a torso model. SIAM Review 2010; 52:717–743.
12. Ten Tusscher KHWJ, Noble D, Noble PJ, Panfilov AV. A model for human ventricular tissue. Am J Physiol 2004; 286:H1573–H1589.
13. Ten Tusscher KHWJ, Hren R, Panfilov AV. Organization of ventricular fibrillation in the human heart. Circ Res 2007; 100:e87–e101.
14. Durrer D, van Dam RT, Freud GE, Janse MJ, Meijler FL, Arzbaecher RC. Total excitation of the isolated human heart. Circulation 1970; 41:899–912.
15. Glukhov AV, Fedorov VV, Lou Q, Ravikumar VK, Kalish PW, Schuessler RB, Moazami N, et al. Transmural dispersion of repolarization in failing and nonfailing human ventricle. Circ Res 2010; 106:981–991.
16. Winslow RL, Greenstein JL, Tomaselli GF, O'Rouke B. Computational models of the failing myocyte: Relating altered gene expression to cellular function. Phil Trans R Soc A 2001; 359:1187–1200.
17. Herweg B, Ilercil A, Madramootoo C, Krishnan S, Rinde-Hoffman D, Weston M, Curtis AB, et al. Latency during left ventricular pacing from the lateral cardiac veins: A cause of ineffectual biventricular pacing. Pacing Clin Electrophysiol 2006; 29:574–581.
18. Barber MR, Fischmann EJ. Heart dipole regions and the measurement of dipole moment. Nature 1961; 192:141–142.
19. Modre R, Tilg B, Fischer G, Wach P. Noninvasive myocardial activation time imaging: A novel inverse algorithm applied to clinical ECG mapping data. IEEE Trans Biomed Eng 2002; 49:1153–1164.
20. Ramanathan C, Jia P, Ghanem R, Calvetti D, Rudy Y. Noninvasive electrocardiographic imaging (ECGI): Application of the generalized minimal residual (GMRes) method. Ann Biomed Eng 2003; 31:981–994.
21. Clerc L. Directional differences on impulse spread in trabecular muscle from mammalian heart. J Physiol 1976; 255:335–346.
22. Valderrabano M. Influence of anisotropic conduction properties in the propagation of the cardiac action potential. Prog Biophys Mol Biol 2007; 94:144–168.
23. Helm PA, Younes L, Beg MF, Ennis DB, Leclercq C, Faris OP, McVeigh E, et al. Evidence of structural remodeling in the dyssynchronous failing heart. Circ Res 2006; 98:125–132.
24. Ten Tusscher KHWJ, Panfilov AV. Alternans and spiral breakup in a human ventricular tissue model. Am J Physiol 2006; 291:H1088-H1100.
25. Weber FM, Keller DU, Bauer S, Seemann G, Lorenz C, Dossel O. Predicting tissue conductivity influences on body surface potentials—an efficient approach based on principal component analysis. IEEE Trans Biomed Eng 2011; 58:265–273.
26. Kohl P, Ravens U. Cardiac mechano-electric feedback: Past, present, and prospect. Prog Biophys Mol Biol 2003; 82:3–9.
27. Vetter FJ, McCulloch AD. Mechanoelectric feedback in a model of the passively inflated left ventricle. Ann Biomed Eng 2001; 29:414–426.

28. Jie X, Gurev V, Trayanova N. Mechanisms of mechanically induced spontaneous arrhythmia in acute regional ischemia. Circ Res 2010; 106:185–192.
29. Keller DUJ, Jarrousse O, Fritz T, Ley S, Dossel O, Seemann G. Impact of physiological ventricular deformation on the morphology of the T-wave: A hybrid, static-dynamic approach. IEEE Trans Biomed Eng 2011; 58:2109–2119.
30. Young AA, Frangi AF. Computational cardiac atlases: From patient to population and back. Exp Physiol 2009; 94:578–596.

Supporting Information

Supporting Information may be found in the online version of this article.

Supplementary movie S1. Simultaneous visualization of instantaneous local excitation, depolarization vector, and ECG
Supplementary movie S2. Excitation of the heart and body surface potential of patient #1
Supplementary movie S3. Excitation of the heart and body surface potential of patient #2 without CRT
Supplementary movie S4. Excitation of the heart and body surface potential of patient #2 with CRT
Supplementary movie S5. Excitation of the heart and body surface potential of patient #3 without CRT
Supplementary movie S6. Excitation of the heart and body surface potential of patient #3 with CRT
Supplementary movie S7. Excitation of the heart and body surface potential of patient #4 without CRT
Supplementary movie S8. Excitation of the heart and body surface potential of patient #4 with CRT

Supporting Information may be found in the online version of this article.
(This link will take you to the article abstract.)